Structural and electronic relaxations around substitutional Cr^{3+} and Fe^{3+} ions in corundum

Emilie Gaudry,* Amonmat Kiratisin, Philippe Sainctavit, Christian Brouder, Francesco Mauri, and Aline Ramos
Laboratoire de Minéralogie Cristallographie de Paris, Université Paris 6, Case 115, 4 Place Jussieu, 75252 Paris Cedex 05, France

Andreï Rogalev and José Goulon
European Synchrotron Radiation Facility, BP 220, F-38043 Grenoble Cedex, France
(Received 11 July 2002; revised manuscript received 7 October 2002; published 17 March 2003)

The local arrangement of atoms surrounding a substitutional Cr^{3+} and Fe^{3+} ion in α-Al_2O_3: Cr^{3+} (ruby) and in α-Al_2O_3:(Fe-Ti) (blue sapphire) has been studied experimentally using natural x-ray linear dichroism absorption at the Cr and Fe K edge. The isotropic and dichroic signals have been recorded using single crystals and a reliable method has been applied to remove diffraction peaks. Results given by the analysis of both signals are compared with *ab initio* density functional calculations. This study reveals that the introduction of an impurity ion in the structure leads to relaxations that are very local in nature. The oxygen atoms in the coordination shell relax to an arrangement similar to that for Cr in α-Cr_2O_3 or for Fe in α-Fe_2O_3. Aluminum or oxygen atoms at a farther distance are weakly affected by the presence of the impurity.

I. INTRODUCTION

The color of allochromatic minerals results from minor impurities and is usually interpreted within the framework of ligand field theory. Indeed, the color diversity in minerals doped with the same impurity is explained by a modification of the crystal field, due to a change of the local environment around this impurity. For example, ruby (α-Al_2O_3: Cr^{3+}) and emerald ($Be_3Al_2Si_{16}O_{18}$:Cr^{3+}) are both doped by chromium in the same valence state and in similar octahedral environments, but ruby is red and emerald is green. The difference of color is explained by a smaller ligand field in emerald than in ruby, which is related to a supposed weaker Cr-O bonding in emerald than in ruby.[1] Likewise, a weakening of the ligand field due to a longer Cr-O bond length in eskolaite (α-Cr_2O_3) than in ruby is invoked to interpret the transition of color from red in ruby to green in eskolaite when increasing the chromium proportion in α-Al_2O_3: Cr^{3+}.[2] To enforce these arguments, a precise description of the local environment around an impurity is needed.

On the other hand, the calculation of the optical properties of materials has made great progress recently.[3–6] These calculations use a combination of the GW approximation and the Bethe-Salpeter equation to describe accurately the electronic excitations and the excitonic processes in semiconductors and insulators. However, these methods were not able to calculate the optical spectra of a transition metal impurity. There are two reasons for this failure. First, transition metal impurities exhibit strong electronic correlations, secondly, the crystallographic structure around an impurity in a crystal is not known. The theory of strongly correlated systems improves steadily and a realistic modeling of the optical spectra of transition metal impurities does not appear out of reach. Therefore, an accurate determination of the atomic position around a transition metal impurity becomes an urgent task.

In this paper, we are interested in the local environment around chromium in ruby (α-Al_2O_3: Cr^{3+}) and around iron in α-Al_2O_3: Fe^{3+}. Corundum (α-Al_2O_3) is a transparent and highly insulating material with a wide band gap energy

[measured value of 8.8 eV (Ref. 7)]. When some transition metal impurities substitute for aluminum in the structure, it becomes colored. Ruby is red and α-Al_2O_3: Fe^{3+} is yellow. To investigate the local structure around chromium or iron, we use a powerful experimental technique that not only gives precise metal-oxygen distances in the coordination shell, but gives metal-aluminum second neighbors distances. All these results, with additional density functional calculations, allow us to have a complete picture of the local environment of chromium and iron impurities in α-Al_2O_3.

The crystal structure of α-Al_2O_3 belongs to the space group $R\bar{3}2/c$ or D_{3d}^6, thus making it a uniaxial birefringent material.[8] The rhombohedral unit cell contains two Al_2O_3 species. Aluminum ions are linked to six oxygen ions in a distorted octahedron, with respect to pure octahedral geometry. The ionic radius of the paramagnetic impurities is larger than the ionic radius of aluminum atoms ($r_{Cr^{3+}}=0.615$ Å, $r_{Fe^{3+}}=0.645$ Å, and $r_{Al^{3+}}=0.535$ Å in an octahedral site[9]). This imposes strong relaxation in the material. Since the Al-O bond in corundum is known to be ionocovalent,[10] the relaxation is not simply given by the difference between the ionic radii of the impurity and the aluminum ion. Many studies have been undertaken to determine the angular and radial relaxations. Single crystal x-ray diffraction,[11,12] UV-VIS spectroscopy,[13,14] and EPR spectroscopy[15,16] have shown the existence of such relaxations. However the metal-oxygen (M-O) bond lengths in the coordination shell were not determined, merely the averaged M-O distances. This can hide probable differences between oxygen atoms in the coordination shell. For instance, the mean Cr-O distance in α-Cr_2O_3 is 1.99 Å (Ref. 17) and the mean Fe-O distance in α-Fe_2O_3 is 2.02 Å.[18] (the mean Al-O distance in α-Al_2O_3 is 1.92 Å.[17]) Although the two mean bond lengths are quite similar, the trigonal distortion of the octahedral site in α-Cr_2O_3 is very different from that in α-Fe_2O_3. The two M-O distances in the coordination shell are 1.97 and 2.02 Å in α-Cr_2O_3 while in α-Fe_2O_3 the values are 1.94 and 2.11 Å (they are 1.86 and 1.97 Å in α-Al_2O_3). To determine precisely the positions of

the nearest and next nearest neighbors, x-ray absorption fine structure (XAFS) has been performed at the Cr K edge in powders[19] or single crystals[20] of α-Al_2O_3: Cr^{3+}. The experimental determination of the precise Cr-O distances in α-Al_2O_3: Cr^{3+} powders is difficult to obtain from isotropic EXAFS signals, due to the large amount of parameters needed to account for the fit. In addition, the difference between two fits performed using either one averaged Cr-O distance or two Cr-O_1 and Cr-O_2 distances leads to little improvement of the fit. The extended XAFS (EXAFS) recording of single crystal spectra is difficult due to the presence of diffraction peaks that strongly distort the experimental information.[20] No XAFS experiments have been performed at the Fe K-edge in sapphire. At the same time, relaxation calculations around chromium in ruby have been performed using parametrized[19] or first principles[21] density functional calculations. The results support the existence of the trigonal distortion of the octahedral site of the impurity. No calculation on the structural relaxation around other $3d$ impurities in corundum has been reported to date.

Our goal is to measure very precisely the distances around paramagnetic impurities in α-Al_2O_3. To do that, it is necessary to record XAFS signals on single crystals, despite the presence of unavoidable diffraction peaks. In this study, a powerful experimental technique[22] presented in Sec. II is used to record XAFS spectra of single crystals at the chromium K edge of α-Al_2O_3: Cr^{3+} and at the iron K edge of α-Al_2O_3: Fe^{3+}. The data treatment gives, simultaneously, the isotropic spectra and the dichroic spectra, without any diffraction peak. The isotropic signal is then classically analyzed to yield averaged bond lengths in the coordination shell. To obtain accurate structural information about the impurity site, it is necessary to analyze the dichroic signal, which is more sensitive to the difference of distances between the two types of oxygen atoms in the coordination shell. Such an analysis is not typical, and details are presented in Sec. III. At the same time we have carried out first principles density functional calculations on α-Al_2O_3: Cr^{3+} and α-Al_2O_3: Fe^{3+} (Sec. IV). The calculated M-O and M-Al distances are compared to experimental values. Results are discussed in Sec. V.

II. X-RAY ABSORPTION MEASUREMENTS

In order to examine the local environment around the impurity ions in ruby and sapphire, it is necessary to measure EXAFS signal on single crystals for two independent orientations of the linear x-ray polarization. We also use the dichroic signal, which gives direct evidence of the inequivalence between atoms around the impurity site.

Two types of single crystals synthesized by the Verneuil process are studied. They are rubies (α-Al_2O_3: Cr^{3+}) containing 60 (± 10), 800 (± 30), 10 000 (± 500) wt. ppm of chromium and a sapphire (α-Al_2O_3:Fe,Ti) containing 1500 (± 50) wt. ppm of iron and 750 (± 30) wt. ppm of titanium. These compositions were analyzed using the Cameca Microbeam electron microprobe at the CAMPARIS analytical facility of the Universities of Paris 6/7. A 30 kV acceleration with a 15 nA beam current, defocused to 10 μm, was used.

X-ray intensities were corrected for dead-time, background, and matrix effects using the Cameca ZAF routine. The standards used were α-Al_2O_3, α-Cr_2O_3, and α-Fe_2O_3. The single crystals of ruby were cylindrically shaped (diameter 15 mm and thickness 3 mm). They were cut so that the C_3 axis ([111] direction in the rhombohedral lattice) was orthogonal to the normal of the disk surface. The single crystal of blue sapphire was cut in a similar way with the C_3 axis orthogonal to the normal of the surface. We made the XAFS experiments on synthetic blue sapphire (α-Al_2O_3:Fe,Ti) instead of on yellow sapphire (α-Al_2O_3: Fe^{3+}) because synthetic yellow sapphires (α-Al_2O_3: Fe^{3+}) with high iron concentrations are often strongly inhomogeneous. We assume that the low concentration of titanium compared to that of iron in blue sapphire does not affect the site relaxation around iron.

In doing XAFS measurements on single crystals, one is faced with the problem of very intense diffraction peaks. These arise from either diffracted rays striking a fluorescence detector or from the occurrence of diffraction inside the crystal.[20] These diffraction rays may drag on and have devastating effects on the whole absorption spectrum. Without the use of the rotating sample technique described in the following, many diffraction peaks were present on the XAFS signal, comparable to what was found by Emura *et al.*[20] These diffraction peaks forbade any unambiguous EXAFS analysis.

In this study, the chromium K edge (energy range 5900–6700 eV) in rubies and the iron K edge (energy range 7050–7500 eV) in sapphire have been measured on the ID12A beam line (European Synchrotron Radiation Facility, France) dedicated to polarization dependent spectroscopies.[23] A special technique called the rotating sample technique, proposed by Goulon,[22] is applied to register the absorption spectra. It is an unusual but powerful method to eliminate diffraction peaks and to measure natural linear dichroism on single crystals. The monochromatic x-ray beam is obtained through a double Si(111) crystal monochromator, having a resolution $\Delta E/E \sim 10^{-4}$. The photon flux is linearly polarized with the polarization vector $\vec{\epsilon}$ orthogonal to the normal of the sample surface. Single crystals are placed on a rotating holder that allows for the samples to be rotated around the x-ray beam direction, perpendicular to the face of the sample. The [111] direction stays perpendicular to the x-ray beam direction when the samples are turned. For each energy $\hbar\omega$ of incident photon, the fluorescence intensity is measured by eight detectors for 400 angles of the rotating holder from 0 to 2π radians. This process is carried out for 700 energy points. Then, the isotropic spectra and the linear dichroism have to be extracted from this amount of data. A filtering algorithm[24] is used to obtain, simultaneously, both the isotropic absorption coefficient μ_{iso} and the dichroic signal μ_{dichro}. This algorithm operates as follows.[24] The experimental dependence of the intensity recorded by each detector at each energy $\hbar\omega$ as a function of angle is fitted to the function

$$f(\theta, \hbar\omega) = a(\hbar\omega) + b(\hbar\omega)\cos\theta + c(\hbar\omega)\sin\theta$$
$$+ d(\hbar\omega)\cos 2\theta + e(\hbar\omega)\sin 2\theta, \qquad (1)$$

where θ is the rotation angle. This function takes various phenomena into account. The dependence on $\cos\theta$ and $\sin\theta$ describes the fact that the x-ray beam is not circular, and that the rotation axis of the sample holder might not be perfectly aligned with the x-ray beam direction. In principle, the spectrum averaged over angles is given by $a(\hbar\omega)$, and the angular dependence is given by $d(\hbar\omega)$ and $e(\hbar\omega)$. It must be checked that $b(\hbar\omega)$ and $c(\hbar\omega)$ are small and do not vary much with $\hbar\omega$. For each detector and each energy, the function $f(\theta,\hbar\omega)$ is first fitted to all of the data (i.e., intensities as a function of angle). A root mean square error σ, between fit and data is obtained. Then, each data point i is in turn selected from the experimental data. A fit is calculated skipping point i and the corresponding root mean square error σ_i is calculated. The experimental point i_0, causing the largest error, is determined by choosing i_0 such that σ_{i_0} is the smallest among the σ_i. Then, σ_{i_0}/σ is calculated. If the ratio is greater than 0.95, it is considered that the fit is not significantly improved by suppressing any point in the data, and therefore the data is taken to be correct. If the ratio is smaller than 0.95, then point i_0 is removed from the experimental data and the process is started again. Once the filtering procedure is finished, the functions $a(\hbar\omega)$, $b(\hbar\omega)$, $c(\hbar\omega)$, $d(\hbar\omega)$, and $e(\hbar\omega)$ of all of the detectors are then summed over. The experimental signal may be written as

$$S(\theta,\hbar\omega)=S_a(\hbar\omega)+S_b(\hbar\omega)\cos\theta+S_c(\hbar\omega)\sin\theta$$
$$+S_d(\hbar\omega)\cos 2\theta+S_e(\hbar\omega)\sin 2\theta. \qquad (2)$$

Given that α-Al_2O_3 is uniaxial, with an appropriate choice for the origin of θ, $S_e(\hbar\omega)$ can be reduced almost to null so that the isotropic part of the signal is $[3S_a(\hbar\omega)-S_d(\hbar\omega)]/3$ and $2S_d(\hbar\omega)$ is the dichroic XAFS signal.[25]

III. EXAFS ANALYSIS

The measured isotropic and dichroic x-ray absorption spectra from the 10 000 wt. ppm Cr^{3+} and 1500 wt. ppm Fe^{3+} doped alumina samples are reproduced in Figs. 1 and 2. We have also measured the EXAFS signal of the other two α-Al_2O_3: Cr^{3+} single crystals with chromium concentration equal to 800 and 60 wt. ppm. The Cr K-edge EXAFS signals of the three α-Al_2O_3: Cr^{3+} samples are essentially identical, except for signal to noise ratio. We also measured the XANES spectra for the three chromium concentrations. It appears that the chromium site must be largely independent of the chromium concentration in a range between 60 and 10 000 wt. ppm. In the following, the EXAFS analysis is performed on the 10 000 wt. ppm α-Al_2O_3: Cr^{3+} and the 1500 wt. ppm α-Al_2O_3:(Fe-Ti) samples.

Given that the isotropic signal is not very sensitive to the small difference between the two M-O distances in the coordination shell, structural information determined by its analysis only gives an averaged picture. The interesting point is the analysis of the dichroic spectra, which provides accurate results concerning the inequivalence between atoms.
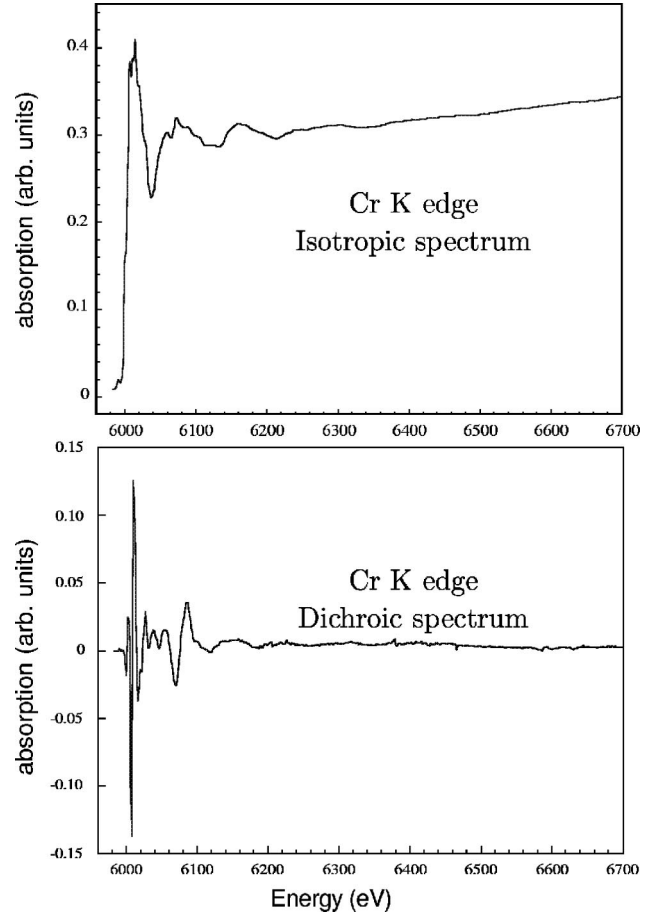

FIG. 1. Isotropic (top) and dichroic (bottom) x-ray absorption spectra (K edge) for Cr in ruby.

A. Isotropic signal

A standard procedure is used to analyze the isotropic part of the two absorption spectra.[26,27] The preedge background is removed by applying a polynomial fit to the pre-edge data and extrapolating it into the post-edge region. Data normalization and energy shift is performed using an error function (step function) and a pseudo-Voigt function (peak function). The energy scale is converted to reciprocal space units using $k=(1/\hbar)\sqrt{2m(E-E_0)}$, where E_0 is the threshold energy of the absorption edge. Then, a cubic spline function is fitted to the k^n weighted data by a non linear least square fit of the spline knots. These normalized EXAFS signals $\chi(k)$ are further analyzed as a Fourier series of plane wavelets. Each has a scattering amplitude of A_j, a back-scattering function $F_j(k)$ and a total phase function $\Phi_{ij}(k)=2\delta_1'(k)+\theta_j(k)$. The first term $\delta_1'(k)$, arises from the potential of the central atom and $\theta_j(k)$ is the phase function of the neighboring atoms[28]

$$\chi(k)=-\frac{1}{k}\sum_j A_j\sin[2kr_j+\Phi_{ij}(k)]. \qquad (3)$$

The summation is over j shells and the scattering amplitudes A_j, are related to the electron mean free path $\lambda_j(k)$, the
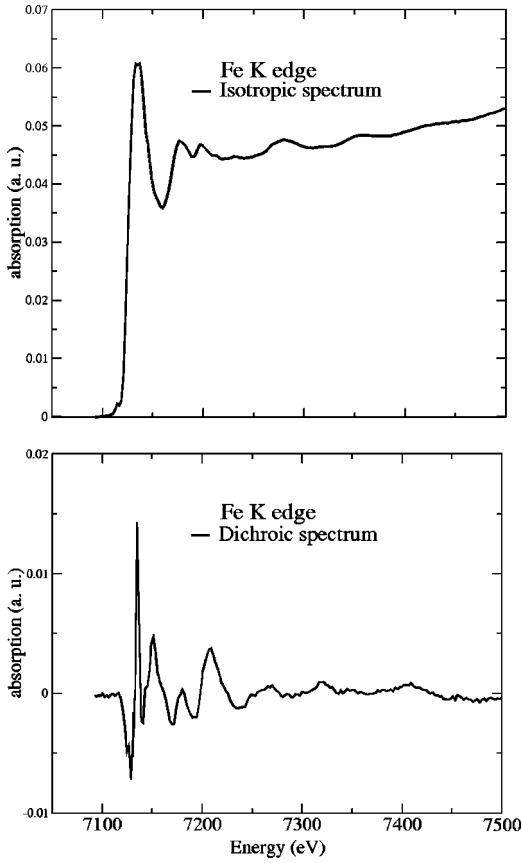
FIG. 2. Isotropic (top) and dichroic (bottom) x-ray absorption spectra (*K* edge) for Fe in sapphire.

FIG. 3. Fourier back-transformed data $k^3\chi(k)$ for Cr in ruby.

coordination number N_j, the bond distances r_j, and the Debye-Waller factor σ_j:

$$A_j = \frac{N_j}{r_j^2} F_j(k) e^{-2\sigma_j^2 k^2} e^{-2r_j/\lambda_j(k)}. \qquad (4)$$

The radial structure function in real space $F(r)$, is obtained by the Fourier transform of the $\chi(k)$ spectra, using the equation $F(r) = (1/2\pi)\int_{k_{min}}^{k_{max}} W(k)k^n\chi(k)e^{2ikr}dk$, where $W(k)$ is a Kaiser window function to minimize truncation effects in the Fourier transform.[29]

We are interested in the determination of structural parameters of both the first shell (*M*-O bonding) and the second shell (*M*-Al bonding). We carry out the analysis in two steps. First we select an *r* range in which only *M*-O contributions are expected and we separate these EXAFS oscillations from the total experimental signal using back Fourier transform. It is well known that in α-Al_2O_3, the six Al-O distances in the first coordination shell are gathered in two groups to comply with the C_3 symmetry. In addition, EPR measurements suggest that the chromium site in α-Al_2O_3: Cr^{3+} is trigonal.[30] Then, the isotropic signal is analyzed with one mean metal-oxygen distance for the fit. The fit gives initial information on N_j, r_j, σ_j and ΔE_0^j that can be useful for the second step. For the second stage, the same separation
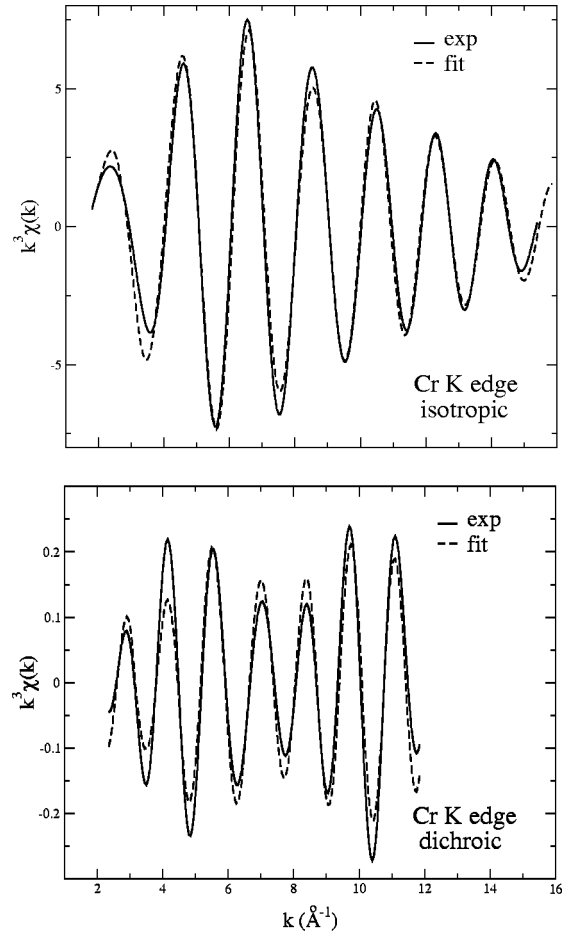
and fit procedure is applied to determine structural information on both the first shell (*M*-O bonding) and the second shell (*M*-Al bonding). In fact, it is very difficult to separate the *M*-O contribution from the *M*-Al because of the displacement of peak positions due to phase shifts $\Phi_{ij}(k)$. The EXAFS oscillations of particular interest are separated from the total experimental signal by a back Fourier transform of the signals. This gives a signal (solid line in Figs. 3 and 4) that can be fitted by a model function (dotted line in Figs. 3 and 4).

B. Dichroic signal

The analysis of the dichroic signal is novel. In keeping with the formalism developed in the preceding paragraph, it is necessary to turn the linear dichroic absorption coefficient $\mu_{dichro}(k)$ into a $\chi_{dichro}(k)$ signal

$$\chi_{dichro}(k) = \frac{\mu_{dichro}(k)}{\mu_0(k)} = \frac{\mu_\parallel(k) - \mu_0(k)}{\mu_0(k)} - \frac{\mu_\perp(k) - \mu_0(k)}{\mu_0(k)}. \qquad (5)$$

We consider a fully linearly polarized x-ray beam.[31] The normalized dichroic EXAFS signal is then given by[28]
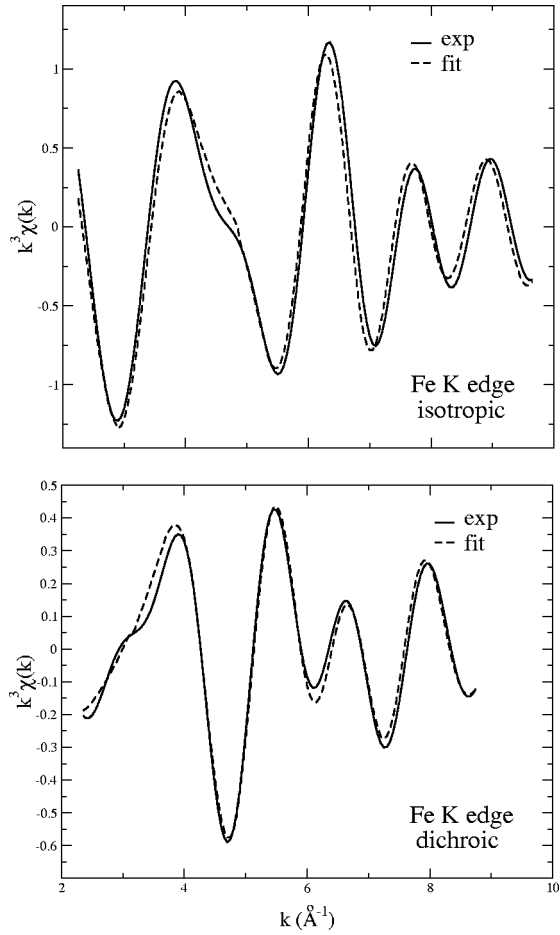
FIG. 4. Fourier back-transformed data $k^3\chi(k)$ for Fe in sapphire.

$$\chi_{\text{dichro}}(k) = -\frac{1}{k} \sum_j A'_j \sin[2kr_j + \Phi_{ij}(k)], \qquad (6)$$

where

$$A'_j = \frac{3N_j}{r_j^2} F_j(k) e^{-2\sigma_j^2 k^2} e^{-2r_j/\lambda_j(k)} [\langle(\hat{\epsilon}_\parallel \cdot \hat{r}_j)^2\rangle - \langle(\hat{\epsilon}_\perp \cdot \hat{r}_j)^2\rangle] \qquad (7)$$

and $\hat{\epsilon}_\parallel$ and $\hat{\epsilon}_\perp$ are unit vectors in the [111] direction and a perpendicular direction ($[\bar{1}2\bar{1}]$, for example), $\langle(\hat{\epsilon}\cdot\hat{r}_j)^2\rangle$

$= 1/N_j \Sigma_i (\hat{\epsilon}\cdot\hat{r}_j^i)^2$ with i running over atoms in the jth shell. Let us introduce $N'_j = 3N_j[\langle(\hat{\epsilon}_\parallel \cdot \hat{r}_j)^2\rangle - \langle(\hat{\epsilon}_\perp \cdot \hat{r}_j)^2\rangle]$. Equation (6) becomes

$$\chi_{\text{dichro}}(k) = -\frac{1}{k} \sum_j \frac{N'_j}{r_j^2} F_j(k) e^{-2\sigma_j^2 k^2} e^{-2r_j/\lambda_j(k)} \sin[2kr_j$$
$$+ \Phi_{ij}(k)]. \qquad (8)$$

Equation (8) is similar to Eq. (3) in the case of an isotropic signal except that N'_j is no longer a positive integer representing a number of atoms. The parameter N'_j is fixed by the geometry and it can be positive or negative. In C_3 symmetry, the shell of neighbors are clustered in packs of three atoms, for which the angle θ_j between the bond $\hat{r}_j$ and the C_3 axis is constant. For such a shell, $N'_j = \frac{3}{2}(3\cos^2\theta_j - 1)$. The dichroic signal $\chi_{\text{dichro}}(k)$ is further analyzed as a Fourier series of plane wavelets with the same technique described in Sec. III A (see Figs. 3 and 4). Because the number of parameters used to fit the experimental spectrum is large, the numbers of neighbors N_j is fixed (3 O_1, 3 O_2, 1 Al_1, and 3 Al_2). The Debye Waller factors σ_j, are fitted, however, we impose $\sigma_{O_1} = \sigma_{O_2}$ and $\sigma_{Al_1} = \sigma_{Al_2}$. The mean free paths are also fitted but we constrain $\lambda_{O_1} = \lambda_{O_2}$ and $\lambda_{Al_1} = \lambda_{Al_2}$. Finally, the inner potential shift ΔE_0^j is fitted, where we set $\Delta E_0^{O_1} = \Delta E_0^{O_2}$ and $\Delta E_0^{Al_1} = \Delta E_0^{Al_2}$. Final results are shown in Tables I and II.

IV. COMPUTATIONS

The structure relaxation calculations were performed using the density functional theory and the local spin density approximation (LSDA) with the parametrization of Ref. 32. We described the atomic cores by norm conserving pseudopotentials[33] in the Kleinman-Bylander form.[34] For the aluminum pseudopotential we considered $1s$, $2s$, and $2p$ as core states, and $3s$, $3p$, $3d$ as valence states with the $3s^2 3p^0 3d^0$ configuration and with core radii of 2.00 atomic units. For the oxygen pseudopotential we considered $1s$ as core state, and $2s$ and $2p$ as valence states with core radii of 1.45 a.u. and with the $2s^2 2p^4$ configuration. For the chromium pseudopotential we considered $1s$, $2s$, $2p$ as core states and $3s$, $3p$, and $3d$ as valence states with core radii of

TABLE I. Distances Cr-O and Cr-Al (Å) from the analysis of the isotropic and dichroic signals and from calculation. These distances are compared to Al-O and Al-Al distances in α-Al_2O_3 and to Cr-O and Cr-Cr in α-Cr_2O_3.

	Al_2O_3 Ref. 17	Al_2O_3: Cr^{3+} isotropic data	Al_2O_3: Cr^{3+} dichroic data	Al_2O_3: Cr^{3+} *ab initio* data	Cr_2O_3 Ref. 17
M-O_1	1.86	1.97	1.92	1.95	1.97
M-O_2	1.97	1.97	2.01	2.00	2.02
M-Al (face)	2.65	2.76	2.65	2.64	2.65
M-Al (edge)	2.79	2.76	2.85	2.80	2.89

TABLE II. Distances Fe-O and Fe-Al (Å) from the analysis of the isotropic and dichroic signals and from calculation. These distances are compared to Al-O and Al-Al distances in α-Al$_2$O$_3$ and to Fe-O and Fe-Fe in α-Fe$_2$O$_3$.

	Al$_2$O$_3$ Ref. 17	Al$_2$O$_3$: Fe^{3+} isotropic data	Al$_2$O$_3$: Fe^{3+} dichroic data	Al$_2$O$_3$: Fe^{3+} *ab initio* data	α-Fe$_2$O$_3$ Ref. 18
M-O$_1$	1.86	2.01	1.90	1.92	1.94
M-O$_2$	1.97	2.01	2.05	2.10	2.11
M-Al (face)	2.65	2.85	2.70	2.72	2.90
M-Al (edge)	2.79	2.85	3.04	2.83	2.97

1.00 (3s) a.u. and 1.70 a.u. (3p and 3d), and with the $3s^2 3p^6 3d^3$ configuration. For the iron pseudopotential we considered 1s, 2s, 3s as core states and 3s, 3p, 3d as valence states with core radii of 0.90 a.u. (3s) and 1.50 a.u. (3p and 3d), and with the $3s^2 3p^6 3d^5$ configuration. Since we have treated 3s, 3p, and 3d as valence states in Fe and Cr, we do not need to include nonlinear core corrections. We expanded the wave functions and the charge density in plane waves with a 80 Rydberg cutoff and a 320 Rydberg cutoff, respectively. The cell used in the density functional calculations was a supercell built on the vectors $2\vec{a}_R$, $2\vec{b}_R$, $2\vec{c}_R$ ($\vec{a}_R$, $\vec{b}_R$, $\vec{c}_R$ are the base vectors of the rhombohedral unit cell) and contained 80 atoms as follows, 1 chromium or iron atom, 31 aluminum atoms, and 48 oxygen atoms. The lattice constants are those resulting from the calculation of Duan *et al.*:[35] a_R = 9.66 a.u. (5.11 Å) and θ = 55.41°. We start the relaxation with aluminum atoms at $\pm(u,u,u;u+\frac{1}{2},u+\frac{1}{2},u+\frac{1}{2})$ where u = 0.352, and with oxygen atoms at $\pm(u,\frac{1}{2}-u,\frac{1}{4};\frac{1}{2}-u,\frac{1}{4},u;\frac{1}{4},u,\frac{1}{2}-u)$ where u = 0.555. The supercell is large enough to minimize interaction between two paramagnetic ions: the minimal distance between two of them is 10.43 Å. The spin multiplet degeneracy imposed on the trivalent paramagnetic ions was 4 for Cr^{3+} and 6 for Fe^{3+}. The Brillouin zone was sampled at the Γ point. We verified the convergence of this calculation by making the difference with a 8 k points computation. The difference between the two calculations is very small since the discrepancies in the atomic forces are less than 0.0015 Ry/a.u. Atomic relaxations were carried out with Car-Parrinello molecular dynamics and simulated annealing. All atoms were allowed to relax. The calculations were performed with the CPMD program.[36] The calculated metal-oxygen and metal-aluminum distances are presented in Tables I and II. Our results for the chromium impurity are similar to those obtained in Ref. 21 using the local density approximation.

V. DISCUSSION

A. Experimental analysis

Our ultimate purpose is the determination of the precise environment of a paramagnetic impurity present in a crystal of corundum. To do so, we have analyzed two independent sets of experimental data (isotropic and dichroic EXAFS spectra) and performed *ab initio* density functional calcula-

tions. The ionic radius for chromium [$r_{Cr^{3+}}$ = 0.615 Å (Ref. 9)] and iron ($r_{Fe^{3+}}$ = 0.645 Å) are almost similar and much larger than the ionic radius for aluminum ($r_{Al^{3+}}$ = 0.535 Å). One then expects the averaged bond distance between the paramagnetic ion and oxygen atoms to be greater than the aluminum-oxygen bond distance in α-Al$_2$O$_3$. This effect has been captured successfully by the isotropic EXAFS. From the conventional analysis of the isotropic signal, it has been possible to extract an averaged Cr-O and Fe-O distance in the coordination shell. We found the Cr-O and the Fe-O mean distances to be 1.97 and 2.01 Å respectively. This is in good agreement with what is expected from the simple application of the ionic radii and also from other data reported in the literature.[11,12,19,37,38] From EXAFS analysis, Emura *et al.*[20] and Kizler *et al.*[19] found the averaged Cr-O distances in ruby to be 2.00 and 1.96 Å. From optical measurements interpreted in the framework of the ligand field multiplet approach, Langer[14] found that the averaged Cr-O distance was about 1.96 Å. Density functional calculations results from this work also yield mean cation-oxygen distances to be in agreement with our isotropic EXAFS data.

In order to experimentally determine the bond distances around the paramagnetic impurities, the analysis of the dichroic EXAFS signal is essential. This is best seen in Fig. 5 where the calculated isotropic and dichroic EXAFS signals using FEFF8 (Ref. 39) program have been represented for three different chromium environments described in the following and labeled cluster 1, 2, and 3. The three clusters contain seven atoms (one chromium atom and six oxygen atoms). The geometry in cluster 1 is given by the density functional calculations results (Sec. IV). It is built with three oxygen neighbors at 1.95 Å making an angle of 62.8° with the C_3 axis and a further three at 2.00 Å with an angle of 48.4°. In cluster 2, the chromium-oxygen bond angles are the same as for the preceding cluster and the bond distances for the six oxygen are set to the averaged value 1.975 Å. In cluster 3, the chromium atom is at the center of a pure oxygen octahedron (1.975 Å for the Cr-O bond lengths) and the dichroic EXAFS signal is zero (at least in the electric dipole approximation). One sees that dichroic EXAFS signals are much more sensitive to differences between chromium-oxygen bonds in the coordination shell than the isotropic signals. This proves that inequivalences between oxygen at-
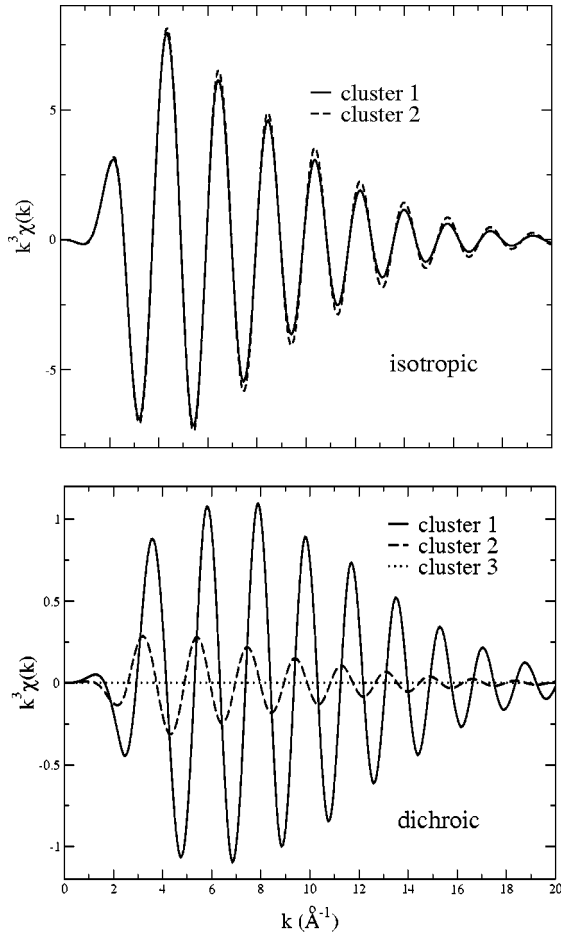
FIG. 5. Calculated isotropic and dichroic EXAFS signals of CrO_6 clusters. These clusters are made of seven atoms (one chromium atom and six oxygen atoms). Cluster 1 is given by density functional calculations (three oxygen atoms at 1.95 Å making an angle of 62.85° with the C_3 axis and three other at 2.00 Å with the angle 48.36°). In cluster 2, the Cr-O bond angles are the same as in cluster 1 and the bond distances for the six oxygen atoms are set to the averaged value 1.975 Å. Cluster 3 is a perfect octahedral cluster (1.975 Å for the Cr-O bond lengths).

oms can reliably been addressed only through the EXAFS analysis of the dichroic signal.

From the dichroic EXAFS signal, it has been found that despite similar mean M-O distances ($M=$ Cr, Fe), the chromium and the iron site in α-Al_2O_3 are very different. If $d_{M\text{-}O_2} - d_{M\text{-}O_1}$ is the difference between the long (M-O_2) and the short (M-O_1) metal-oxygen distances, then $d_{Cr\text{-}O_2} - d_{Cr\text{-}O_1} = 0.09$ Å and $d_{Fe\text{-}O_2} - d_{Fe\text{-}O_1} = 0.15$ Å. From the previous experimental findings, it is clear that the six oxygen

atoms group into two distance groups, thus it is realistic to believe that the C_3 axis of corundum crystal is conserved at the impurity site. This is in agreement with what was found from density functional calculations and also from the EPR measurements in α-Al_2O_3: Cr^{3+}.[30] It should be noted that if two oxygen shells at the two different distances from the central chromium atom, as determined by the analysis of the dichroic EXAFS signal, are introduced in the analysis of the isotropic EXAFS signal, then the experimental signal can be fitted with just a few modifications of the apparent Debye Waller factors. The contribution of the first aluminum neighbors around the paramagnetic impurity can also be determined by the analysis of the dichroic EXAFS signal. There are two types of aluminum neighbors. The first aluminum neighbor is on the C_3 axis in an octahedron joined by a face with the impurity octahedron. The second shell of aluminum neighbors consist of three ions in an octahedron, joined by three edges with the impurity octahedron. This strongly anisotropic distribution yields a large contribution to the dichroic EXAFS signal, from which it is possible to determine with a good reliability, the rather large cation-aluminum distances. It is found that for the chromium site, the Cr-Al distances are 2.65 Å for the aluminum on the C_3 axis and 2.79 Å for the three farther aluminum neighbors. In the same way, the Fe-Al distances are determined to be 2.75 Å for the first aluminum atom and 2.88 Å for the three farther aluminum atoms.

From the point of view of EXAFS measurements, our finding gives the following picture for the relaxation around the paramagnetic impurity. The symmetry of the relaxed site for Cr or Fe is compatible with the C_3 point group that is the site symmetry of aluminum atoms in corundum. The local environment around the chromium ion in ruby is nearly the same as that in α-Cr_2O_3. The Cr-O bond lengths in ruby are closer to Cr-O bond lengths in α-Cr_2O_3 rather than to Al-O bond length in α-Al_2O_3 (see Table I). However, Cr-Al (edge) distances are closer to Al-Al bond lengths in α-Al_2O_3 than to Cr-Cr bond lengths in α-Cr_2O_3. The relaxations seem to be very local and do not affect atoms far from the chromium ion, within an error bar of about 1%. The case of iron in corundum is not exactly the same as that of chromium. The Fe-O bond lengths in blue sapphire are closer to the Fe-O bond lengths in α-Fe_2O_3 rather than to Al-O bond lengths in α-Al_2O_3 and the Fe-Al bond lengths are in between Al-Al bond lengths in α-Al_2O_3 and Fe-Fe bond lengths in α-Fe_2O_3. Seen from perspective of the impurity, the relaxation extends farther in α-Al_2O_3: Fe^{3+} than in α-Al_2O_3: Cr^{3+}.

To have a precise description of the site departure from pure octahedral geometry, the parameter τ is constructed. It is defined as $\tau(M) = 200[(d_{M\text{-}O_2} - d_{M\text{-}O_1})/(d_{M\text{-}O_2} + d_{M\text{-}O_1})]$.

TABLE III. Departure from pure octahedral geometry. The r_+ and the r_- distances are the M-O_2 and M-O_1 distances, respectively.

	Al_2O_3 Ref. 17	Al_2O_3: Cr^{3+} dichro.	calc.	Cr_2O_3 Ref. 17	Al_2O_3: Fe^{3+} dichro.	calc.	α-Fe_2O_3 Ref. 18
$\dfrac{2(r_+ - r_-)}{r_+ + r_-}100$	5.74	4.58	2.53	2.51	7.59	8.96	8.40

It is clear from Table III that $\tau(\mathrm{Cr}^{3+}) < \tau(\mathrm{Al}^{3+}) < \tau(\mathrm{Fe}^{3+})$ in $\alpha\text{-Al}_2\mathrm{O}_3$. In fact, the spectroscopic term of the ground state of Cr^{3+} is ${}^4A_{2g}$ and it is ${}^6A_{1g}$ (essentially from ${}^6S$ spherical spectroscopic term) for Fe^{3+}. The crystal field is then expected to have less impact on the ${}^6A_{1g}$ term than on the ${}^4A_{2g}$ term. The Fe^{3+} ground state energy is almost independent of the crystal field, so that large lowering of symmetry has almost no influence on the Fe^{3+} ion. On the contrary, the ${}^4A_{2g}$ term is affected by the crystal field and $\tau(\mathrm{Cr}^{3+}) < \tau(\mathrm{Al}^{3+})$. The determination of the impurity site departure from pure octahedral symmetry is worthwhile concerning the color. Ruby or $\alpha\text{-Al}_2\mathrm{O}_3$: Fe^{3+} presents two distinct colors depending on the angle of the polarization vector of light with the C_3 axis. This property of dichroism goes directly with the two kinds of metal-oxygen distances in the coordination shell. Their precise determination is essential for next optical spectra calculations.

When considering distances extracted from EXAFS data, all the distances around the impurity are centered around the impurity site. This can hide the actual size of the perturbation imposed by the impurity. This is what has been examined in the following section.

B. Size of the relaxation around the paramagnetic impurity

We would like to use the density functional calculations results for further analysis regarding information on atoms far from the absorbing atom. Such analysis is unobtainable with EXAFS measurements but can be undertaken successfully with a DFT calculation. From the position of atoms in the supercell given by the density functional calculations, it is possible to generate all possible positions of atoms in a crystal by using lattice translation vectors. This collection of atoms is then sorted by increasing distances from the central atom. At the end, a cluster is obtained by keeping atoms inside a sphere S of radius 5.2 Å. In our computation, the super-cell is such that the shortest impurity-impurity distance is 10.43 Å. It is then reasonable to limit any analysis concerning the size of the relaxation around a specific impurity to a sphere S of radius 5.2 Å around this impurity. In doing so, relaxations imposed by other impurities are minimized.

One needs to compare the relaxed coordinates of atoms in the sphere S to coordinates that equivalent atoms have in the pure corundum structure. This pure corundum structure was obtained by a convergent density functional calculation, starting from the positions given by Duan *et al.*[21] The differences between the converged positions and the initial positions were always less than 0.01 Å. Given that the supercell may be translated and rotated by the DFT calculation, it is necessary to align the relaxed and the pure corundum structure. This is done in a number of steps. First, the atoms of the two clusters are rotated so that the C_3 axis of the two clusters are parallel to the same axis (called z axis). The azimuthal angle is determined so as to minimize the quantity Q, where Q is the sum over all the atoms P_i inside S of the norms of the displacement vectors $\vec{V}_i$:

$$Q = \sum_i |\vec{V}_i| = \sum_i \sqrt{[X^i_{\mathrm{relax}} - X^i_{\mathrm{unrelax}}]^2 + [Y^i_{\mathrm{relax}} - Y^i_{\mathrm{unrelax}}]^2 + [Z^i_{\mathrm{relax}} - Z^i_{\mathrm{unrelax}}]^2},$$

where X^i_{unrelax}, Y^i_{unrelax}, and Z^i_{unrelax} are the coordinates of the vector joining the central aluminum atom to the neighboring oxygen or aluminum atoms i of the corundum structure and X^i_{relax}, Y^i_{relax}, and Z^i_{relax} are the respective counterparts joining the impurity to the neighboring atoms of the relaxed structure. In doing so, one finds that relaxation in α-$\mathrm{Al}_2\mathrm{O}_3$: Cr^{3+} is small although not negligible (aluminum neighbors at 4.2 Å are moved by 0.04 Å) while in α-$\mathrm{Al}_2\mathrm{O}_3$: Fe^{3+}, the relaxation is larger as aluminum and oxygen neighbors at 4.2 Å are displaced by more than 0.1 Å. Such a middle range relaxation is simply due to the displacement of the impurity itself. To eliminate the influence of the impurity displacement all atoms in the relaxed and unrelaxed clusters are translated so as to superimpose the centers Ω ($\overrightarrow{O\Omega} = \Sigma_i \overrightarrow{OP}_i$ where i runs over all atoms P_i inside the sphere S except the central atom) of the two clusters. The norm of the displacement vector is evaluated again for each atom in sphere S and results are reported in Figs. 6 and 7. With this method, one considers the relaxation as a whole and not merely as seen by the impurity. This is especially important when the impurity is not precisely located at the aluminum site. One sees that the relaxations around Cr or Fe are very local. The oxygen coordination shell absorbs almost all the relaxation. Atoms further than 2.5 Å are displaced by less than 0.035 Å. Relaxation around iron can be described as follows. Iron is repelled by the nearest aluminum neighbor along the C_3 axis. The oxygen coordination shell is strongly relaxed by 0.08 and 0.11 Å, and further neighbors remain almost nondisplaced. That is in line with some previous EPR measurements where Fe is said to be moved by 0.04 Å ± 0.02 Å on the C_3 axis farther from the first aluminum neighbors.[16] Around chromium, the picture is slightly different. The chromium atom is almost at the aluminum site and oxygen atoms of the coordination shell move to accommodate for the larger ionic radius. Again, the relaxation is very local. The literature is controversial concerning the direction of the displacement of the chromium atom along the C_3 axis.[11,12,19,37,38] In all cases the displacement is said to be small. In addition, we have analyzed the angular relaxations. To this end, we evaluate $\delta\theta = \theta_{\mathrm{unrelax}} - \theta_{\mathrm{relax}}$, where θ is the angle between the $\overrightarrow{\Omega P}_i$ direction and the C_3 axis. In both cases, angular relaxation is weak.

Thanks to all of these results, it is now possible to picture the relaxation (see Fig. 6). Chromium as an impurity in α-
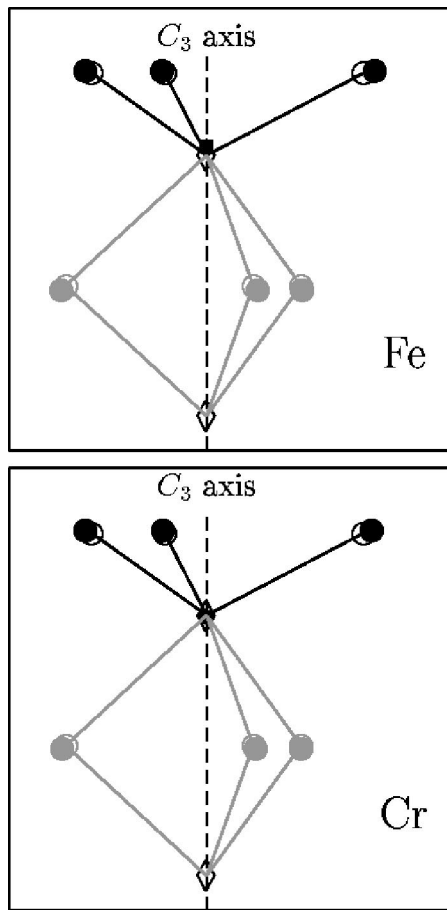
FIG. 6. Environment around the paramagnetic impurity. All atoms are projected on a plane containing the C_3 axis. The circles represent the oxygen atoms, the diamonds the aluminum atoms, the square the impurity atom. Empty signs represent the positions of atoms in α-Al_2O_3, full signs represent the positions of atoms in α-Al_2O_3: Cr^{3+} or in α-Al_2O_3: Fe^{3+}. As seen from the upper picture, the iron atom in α-Al_2O_3: Fe^{3+} does not take exactly the same place as the aluminum ion in α-Al_2O_3.
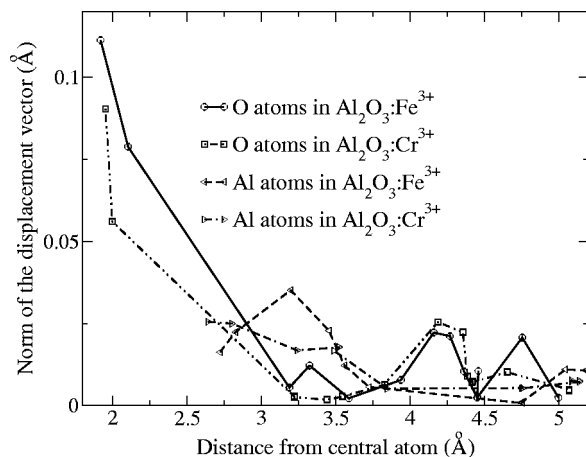
FIG. 7. Relaxations in α-Al_2O_3: Cr^{3+} and α-Al_2O_3: Fe^{3+}. Norms of displacement vectors as a function of distances from the chromium or iron atom.

Al_2O_3 tends to impose the large site it has in α-Cr_2O_3. This mismatch between Al-O_1 bond distances in α-Al_2O_3 and Cr-O_1 bond distances in Cr_2O_3 is $+0.11$ Å and between Al-O_2 and Cr-O_2 it is $+0.05$ Å. In the actual α-Al_2O_3: Cr^{3+} crystal the mismatch is compensated by a displacement of O_1 type atoms by 0.09 Å nearly in the Cr-O_1 bond direction. The O_2 oxygen atoms are displaced by 0.05 Å in the Cr-O_2 bond direction. The same considerations apply to Fe in α-Al_2O_3. The mismatch between Al-O_1 distances in α-Al_2O_3 and Fe-O_1 distances in α-Fe_2O_3 is $+0.08$ Å, while between Al-O_2 and Fe-O_2 it is $+0.14$ Å. The three O_2 type oxygen atoms determine the shared face between Fe and its nearest Al neighbor. A displacement as large as 0.14 Å would considerably shorten Al-O_2 bond lengths and perturb the crystal. For iron to accommodate its relaxed site, it moves away by 0.09 Å along the C_3, axis farther from its nearest Al neighbors with a concomitant displacement of 0.09 Å for O_2 type atoms and 0.11 Å for O_1 atoms. As in α-Al_2O_3: Cr^{3+}, atoms farther than the coordination shell do not move much.

VI. CONCLUSION

Iron and chromium are known to be at the origin of the color of many minerals. In this paper, we have shown that the analysis of the isotropic and dichroic x-ray absorption spectra yields significant information about relaxations around impurities in single crystals. *Ab initio* calculations confirm results given by the experimental analysis and provide an overall view of the relaxation. These structural determinations are an essential first step toward *ab initio* calculations of optical spectra. Concerning ruby, this study contributes to the understanding of the change of color from red to green when increasing the chromium concentration.[40] It is usually believed that the mean metal-ligand distance plays a considerable role in the color process. Contrary to what can be found in textbooks,[1,2] we have shown that the difference of the Cr-O distances in ruby and in α-Cr_2O_3 is not at the origin of the modification of the color. Other parameters such as electron and magnetic pairing between chromium neighbors certainly play a role in the color process. These parameters could for instance be investigated by spectroscopic measurements at chromium $L_{2,3}$ edges.

*Electronic address: emilie.antoine@lmcp.jussieu.fr

[1] K. Nassau, *The Physics and Chemistry of Color* (Wiley, New York, 1983).

[2] R. G. Burns, *Mineralogical Applications of Cristal Field Theory*, Vol. 5 of *Cambridge Topics in Mineral Physics and Chemistry*, 2nd ed. (Cambridge University Press, Cambridge, 1993).

[3] L. X. Benedict, E. L. Shirley, and R. B. Bohn, Phys. Rev. Lett. **80**, 4514 (1998).

[4] S. Albrecht, L. Reining, R. DelSole, and G. Onida, Phys. Rev. Lett. **80**, 4510 (1998).

[5] M. Rohlfing and S. G. Louie, Phys. Rev. B **62**, 4927 (2000).

[6] V. Olevano and L. Reining, Phys. Rev. Lett. **86**, 5962 (2001).

[7] R. H. French, J. Am. Ceram. Soc. **73**, 477 (1990).

[8] J. F. Nye, *Physical Properties of Crystals* (Clarendon, Oxford, 1957).

[9] R. D. Shannon, Acta Crystallogr., Sect. A: Cryst. Phys., Diffr., Theor. Gen. Crystallogr. **32**, 751 (1976).

[10] W. Y. Ching and Y.-N. Xu, J. Am. Ceram. Soc. **77**, 404 (1994).

[11] J. W. McCauley and G. V. Gibbs, Z. Kristallogr. **135**, 453 (1972).

[12] S. C. Moss and R. E. Newnham, Z. Kristallogr. **120**, 359 (1964).

[13] D. S. McClure, J. Chem. Phys. **36**, 2757 (1962).

[14] K. Langer, Z. Kristallogr. **216**, 87 (2001).

[15] R. Büscher, K. P. Such, and G. Lehmann, Phys. Chem. Miner. **14**, 553 (1987).

[16] Z. Wen-Chen, Physica B **245**, 119 (1998).

[17] W. B. Pearson, *Structure Reports* (International Union of Cristallography, Utrecht, 1962), Vol. 27.

[18] L. W. Finger and R. M. Hazen, J. Appl. Phys. **51**, 5362 (1980).

[19] P. Kizler, J. He, D. R. Clarke, and P. R. Kenway, J. Am. Ceram. Soc. **79**, 3 (1996).

[20] S. Emura, H. Maeda, Y. Kuroda, and T. Murata, Jpn. J. Appl. Phys. **32**, 734 (1993).

[21] W. Duan, G. Paiva, R. M. Wentzcovitch, and A. Fazzio, Phys. Rev. Lett. **81**, 3267 (1998).

[22] J. Goulon, C. Goulon-Ginet, A. Rogalev, G. Benayoun, C. Malgrange, and C. Brouder, Proc. SPIE **3773**, 316 (1999).

[23] J. Goulon, A. Rogalev, C. Gauthier, C. Goulon-Ginet, S. Paste, R. Signorato, C. Neumann, L. Varga, and C. Malgrange, J. Synchrotron Radiat. **5**, 232 (1998).

[24] Ch. Brouder, D. Cabaret, Ph. Sainctavit, A. Kiratisin, J. Goulon, and A. Rogalev, Radiat. Eff. Defects Solids **155**, 89 (2001).

[25] C. Brouder, J. Phys.: Condens. Matter **2**, 701 (1990).

[26] M. Winterer, J. Phys. IV **7**, 243 (1997).

[27] D. Bonnin, G. Calas, H. Suquet, and H. Pezerat, Phys. Chem. Miner. **12**, 55 (1985).

[28] B. K. Teo, *EXAFS: Basic Principles and Data Analysis* (Springer Verlag, Berlin, 1985).

[29] D. C. Koningsberger and R. Prins, *X-ray Absorption. Principles, Applications, Techniques of EXAFS, SEXAFS, and XANES* (Wiley, New York, 1988), Vol. 92.

[30] B. Boizot, Ph.D. thesis, Université Paris VI, 1996.

[31] L. Varga, C. Giles, C. Neumann, A. Rogalev, C. Malgrange, J. Goulon, and F. D. Bergevin, J. Phys. IV **7**, 309 (1997).

[32] S. Goedecker, M. Teter, and J. Hutter, Phys. Rev. B **54**, 1703 (1996).

[33] N. Troullier and J. L. Martins, Phys. Rev. B **43**, 1993 (1991).

[34] L. Kleinman and D. M. Bylander, Phys. Rev. Lett. **48**, 1425 (1982).

[35] W. Duan, R. M. Wentzcovitch, and K. T. Thomson, Phys. Rev. B **57**, 10 363 (1998).

[36] J. Hutter, P. Ballone, M. Bernasconi, P. Focher, E. Fois, S. Goedecker, M. Parrinello, and M. Tuckerman (unpublished).

[37] N. Laurance, E. C. McIrvine, and J. Lambe, J. Phys. Chem. Solids **23**, 515 (1962).

[38] L. L. Lohr and W. H. Lipscomb, J. Chem. Phys. **38**, 1607 (1963).

[39] A. L. Ankudinov, B. Ravel, J. J. Rehr, and S. D. Conradson, Phys. Rev. B **58**, 7565 (1998).

[40] D. Reinen, Struct. Bonding (Berlin) **6**, 30 (1969).